JOURNAL OF MATERIALS SCIENCE 37 (2002) 5197–5207

Experimental observations and computer simulations of spherical aluminum-alloy projectiles impacting plane limestone targets

F. M. RANDRIANARIVONY, S. LAIR, S. A. QUINONES, L. E. MURR
Department of Metallurgical and Materials Engineering, University of Texas at El Paso, El Paso, TX 79968, USA
E-mail: fekberg@utep.edu

The stress distribution within spherical aluminum-alloy (2024) projectiles impacting plane limestone (calcite) targets was observed by converting residual microhardness maps obtained for cross-sections of recovered projectiles impacting from 0.8 to 1.3 km/s. A maximum residual yield stress zone was observed to migrate toward the rear of the impacting projectiles with increasing impact velocity. The maximum occurred at a normalized depth $z'/a_m \cong 0.5$ (where a_m is the contact radius); consistent with the theoretical result for elastic impacts. Computer simulations showed good agreement with experiment, and demonstrated that elastic assumptions were valid well into the plastic deformation regime.

1. Introduction

Impacts, including multiple impacts involving very small particles (0.02 to 0.2 mm) have a wide range of interests which encompass ballistic and hypervelocity impacts (with projectile diameters ranging from 0.3 to 30 cm). These can include military targets and a variety of structural systems in space, shot peening to improve the mechanical behavior of surfaces of structural parts, and a variety of cavitation-erosion damage to surfaces. This range of impact produces a wide variety of surface and subsurface damage effects which, on a larger scale, include cratering and deep penetration of structural targets and armor.

Particular interest in many related impact studies centers on the issues of subsurface deformation and residual stresses in the target materials, including the evolution or progression of microstructure [1–6]. In many instances, the surface or near surface region in the impacted, plane target exhibits some softening as a consequence of dynamic recrystallization followed by a hard zone which gradually declines toward the original target hardness [3, 5, 6]. These residual hardness zones increase in size and shift slightly into the target from the impact surface with increasing penetrator velocity, penetrator size, angle of impact, etc. In many studies, contact is characterized simply as the impact of rigid, elastic spheres producing a correspondingly, idealized target geometry, but in actual crater or penetration development, the actual crater geometries may become considerably exaggerated, especially where the projectiles have very large densities (>7 g/cm^3) [7], and severe plastic deformation of both the projectile and target occur.

In many impact systems which are treated as ideally elastic regimes, a maximum residual stress occurs below the impact (or target) surface and moves away from the surface and deeper into the target material with increasing impact velocity [2–5]. The practical implications of elastic regimes include impacts on ceramic or other brittle surfaces which respond elastically up to fracture [8, 9]. However, at sufficiently high velocities for finite target thicknesses, shock-induced spallation and other mitigating issues can intervene, and of course systems which can respond plastically do so. In this context, the impacting particles or projectiles are always of finite dimensions and for spherical projectiles the geometry is particularly unique since from the instant of impact, the associated shock wave (or corresponding peak pressure) propagating through the projectile successively reflects from its surface. In addition, the impacting projectile can undergo plastic deformation which, at sufficiently high impact velocities can contribute to projectile flow and fragmentation. At hypervelocities, some impacting projectiles are often considered to melt or vaporize during crater formation.

In retrospect, very little is known about the behavior of impacting projectiles, and in some cases this may be even more important than the target behavior. The issues of interest involve the development and movement of residual stresses in the impacting projectile with increasing impact velocity and the role these residual stresses may play in the actual deformation and fate of the projectile. Since the projectile has a finite volume and idealized spherical shape at the outset, it can serve macroscopically and microscopically as both a quantitative and qualitative measure of elastic or elastic-plastic behavior.

It is the intent of this study to examine idealized, spherical projectiles which have impacted relatively brittle/ceramic limestone targets over a range of impact

velocities in order to validate computer simulations allowing for extrapolations and observations of the behavior of these projectiles over a range of low impact velocities; which include progressions from the onset of plastic deformation. The intent is therefore to examine the occurrence of a maximum residual stress and its disposition and migration in a finite projectile regime with impact velocity.

2. Elastic impact implications: elasticity theory predictions

Initial impact on a surface is purely elastic followed by an elasto-plastic response and finally severe plastic deformation of both the penetrating projectile and the target surface. Deformation analysis based on elasticity theory provides the basis for elementary dislocation theory and an understanding of residual stresses in bodies as a consequence of tractable solutions based on linear stress-strain relationships. In essentially all impact considerations, the approach involves the determination of residual (elastic) stresses below the impact (target) surface-invariably considered to be a plane section or half section which further assures linearity.

For normal impact of a spherical projectile of radius R, density ρ_p and modulus of elasticity E_p impacting a plane target material having a Poisson ratio, ν_t at a velocity v as illustrated in Fig. 1a for the purely elastic case, the (elastic) indentation as measured by contact radius, a_m in Fig. 1a is given by [10–12]:

$$a_m = 2.5\pi\rho_p\left(1-\nu_t^2\right)\Big/E_p^{1/5}Rv^{2/5}. \tag{1}$$

For a uniform load intensity of [8, 10]:

$$q = 3\rho_p v^2/4, \tag{2}$$

the maximum shear stress τ_m, along the impact axis (Fig. 1a) and at a depth z below the plane target surface can be given by [8]:

$$\tau_m = \frac{q}{2}\Bigg[(1-2\nu_t)+2z(1+\nu_t)\left(a_m^2+z\right)^{-1/2} - \frac{3}{2}z\left(a_m^2+z^2\right)^{-3/2}\Bigg]; \tag{3}$$

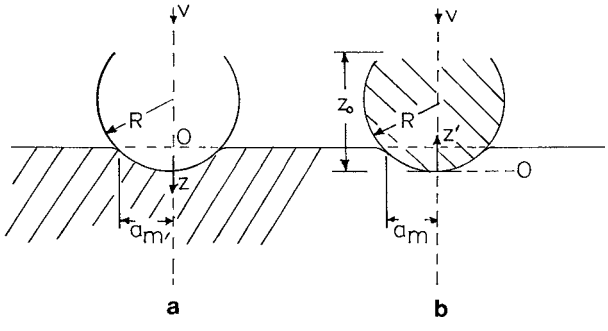

Figure 1 Geometry employed in the computations modelling impacting projectiles embedded in a plastically deformed envelop which elastically indents on the underlying material: (a) Plane surface deformation. (b) Impacting spherical projectile deformation. Distance from the target reference surface is denoted z in (a) while distance into the projectile along the impact axis (dotted) is denoted z' in (b).

which has a local maximum, τ_{max}, at a distance z_{max} below the surface [10]. Beyond z_{max}, the shear stress decreases with depth, z. This maximum residual stress phenomenon has recently been observed for sub-surface stresses accompanying particle erosion wear [14], residual stresses below shot-peened surfaces [15], and ceramic target surfaces impacted by ballistic rods [8].

In the present study, we are interested in assessing this residual stress phenomenon in a spherical, impacting projectile as illustrated schematically in Fig. 1b. Here the contact radius is the same as in Fig. 1a and represented by Equation 1. The load intensity in the impacting sphere is also assumed to be the same as given in Equation 2; especially when the impacting projectile and the target have the same density ($\rho_p \cong \rho_t$). Correspondingly, the maximum shear stress along the impact axis at a distance z' from the contact point at 0 in Fig. 1b is approximated by Equation 3. Consequently, a local maximum shear stress will also occur within the projectile at some distance z'_{max} from the contact point shown in Fig. 1b. In effect, the impacting sphere should exhibit a migrating zone between a plastic (or heavily deformed) surface layer within the contact zone ($2a_m$ in Fig. 1b) and the overlying material; which will exhibit the saturation hardness.

Residual stress ($\sigma_y = \tau_m/M$; where M is the Schmid Factor), in a large, impacting projectile can be determined in metals such as aluminum or aluminum alloys by measuring residual hardness, H, since $\sigma_y \cong H/3$. Consequently, cutting impacted spheres in half and mapping the hardness over the surface of the half section can provide an experimental representation of the residual stress.

The examination of impacting spheres on a target can have special features and advantages in examining residual stress phenomena because ideal, macroscopic strains can be determined from the residual shape changes. The spherical projectile represents an idealized, finite volume whose half-section is representative of a 2-dimensional plane circle area which can be ideally simulated using 2-D computational analysis. Consequently, experimental validation of the experimental regime can allow extrapolations to interrogate a wide range of elastic-plastic deformation behavior associated with impact. Finally, the applicability of elasticity theory and the development and variations of residual stress profiles can be examined in a simple, finite, geometrical solid.

3. Experimental details

Spherical aluminum alloy (2024) projectiles (with a density of 2.8 g/cm^3) and 1.9 cm in diameter were machined and polished from commercial wrought plate. These projectiles were launched from a 40 mm powder gun utilizing a plastic sabot system against thick (semi-infinite) polished limestone targets (polycrystalline calcium carbonate with a density of approximately 2.7 g/cm^3). Three experiments involving impact velocities of 0.8, 1.0, and 1.3 km/s were conducted in which the impacted aluminum alloy projectiles were retrieved. These projectiles were cut exactly in half

(one exact half) and embedded in a standard embedding medium which allowed them to be polished and etched (using a Keller's reagent) to examine the microstructure by optical metallography, and perform a series of microhardness measurements over the entire half section in order to produce residual hardness (or corresponding stress) maps of the half section. Digital, automated Vickers microhardness measurements were made on the polished and etched half sections utilizing a 50 gf (0.5 N) load in a Shimadzu HMV-2000 hardness tester. A corresponding hardness map was also produced for an original, unimpacted spherical projectile along with observations of the original grain structures.

Selected specimens for transmission electron microscopy (TEM) were prepared by taking thin sections from slices made on the corresponding half-sections of the original and impacted spheres. Selected slices cut using a diamond saw were ground to thicknesses of roughly 0.2 mm thick and standard 3 mm TEM discs punched from specific locations corresponding to the hardness maps; or specific hardness zones characterized by the maps. These discs were electropolished in a Tenupol 3-jet polisher using a solution of 1.2 L methanol and 0.3 L nitric acid; at -20°C. The electron transparent thin sections were then observed in a Hitachi H-8000 analytical TEM operated at 200 kV accelerating potential; utilizing a goniometer-tilt stage.

TABLE I Material input parameters

Parameter	Calcite (soda-lime glass) target	Aluminum 2024 projectile
Equation of state	Linear	Shock
Strength model	von Mises	Johnson-Cook
Density (g/cm^3)	2.74	2.785
Bulk modulus (Mbar)	0.43	–
Shear modulus (Mbar)	0.15	0.276
Reference temperature (K))	300	300
Yield stress (Mbar)	1.5×10^{-3}	2.76×10^{-3}
Hardening constant (Mbar)	–	4.26×10^{-3}
Hardening exponent	–	0.34
Strain rate constant	–	0.015
Thermal softening	–	1
Exponent melting temperature (K)	–	775

TABLE II Grid input parameters

Parameter	Grid
Processor	Euler
Symmetry	Axial
Standard units (length, mass, time)	cm, g, μs
Dimensions	10 cm $\times$ 3 cm
Maximum energy error	0.15
Grid spacing	0.05 cm

4. Computer Modeling Details

Autodyn-2D (version 4.6) hydrocode software was used in calculations and simulations reported in this study and was assumed to accurately describe the projectile cross-sections and corresponding half-section views of the impact process. This software is a relatively simple, interactive, integrated hydrocode available on a PC-compatible disk which has been successfully applied in related impact and penetration research [5, 6].

Depending on the user needs AUTODYN provides four different processors Lagrange, Euler, Arbitrary Lagrange Euler (ALE), and Shell. The Euler processor, which simulates material movement by the transference of material through the subgrid, was used for this study.

The grid size and material variables were set up in the same manner for the range of velocities considered in this problem ($0.65 < v < 1.8$ km/s). The material input data is shown in Table I, and the grid information is shown in Table II.

The equation of state (EOS) and related shock wave and materials properties for calcite (often referred to as Solenhofen limestone) and aragonite have been described in part by Von Thiel *et al.* [16], Tyburczy and Ahrens [17], and Ivanov and Deutsch [18]. However, the lack of complete data required for autodyn simulation, and a consideration of the fact that we were only concerned with the target as an impact substrate, led to an examination of very similar and more comprehensively described materials data. The material properties and the strength model for soda-lime glass were used as an approximation for the limestone (calcite) target. The value for the density of limestone (Calcite: $\rho_t = 2.74$ g/cm^3) was incorporated into the soda-lime glass data as shown in Table I.

A linear equation of state was used for the target where Hooke's Law is the basis of the equation, which is written as

$$P = K\mu \tag{4}$$

where P is the hydrostatic pressure, μ is the material compression ($\mu = \rho/\rho_o - 1$), and K is the material bulk modulus. The von Mises strength model was chosen for the target. The corresponding equation is of the form

$$\sigma_y = \left\{\left[(s_1-s_2)^2+(s_2-s_3)^2+(s_3-s_1)^2\right]/2\right\}^{1/2} \tag{5}$$

where σ_y is the yield strength and s_1, s_2 and s_3 are components of deviatoric stress.

The aluminum alloy projectile was modeled with a shock equation of state and Johnson-Cook strength model. The shock (Hugoniot) equation of state is based on the Rankine-Hugoniot equations of the general form

$$U = c_o + su_p \tag{6}$$

where U is the shock velocity, u_p is the particle velocity, s an empirical parameter ($\simeq$1.3 for Al 2024 [15]) and c_o is the sound speed. This linear relationship has been found to model most solids that do not undergo a phase change. The Johnson-Cook constitutive model defines yield stress as

$$\sigma_y = \left[A + B\varepsilon_p^n\right]\left[1 + C\log\varepsilon_p^*\right]\left[1 - T_H^m\right] \tag{7}$$

where A, B, C, n and m are material constants, ε_p is the effective plastic strain, ε_p^* is the normalized effective plastic strain rate and T_H^m is the homologous temperature, where

$$T_H^m = (T - T_{room})/(T_{melt} - T_{room}). \quad (8)$$

5. Results and discussion

Fig. 2 shows the cross-sections (half-sections) of the recovered projectiles impacted into limestone targets at velocities noted. Fig. 3 compares grain structures for the unimpacted spherical projectile and regions marked by the arrows near the impact surfaces in Fig. 2a and c which exhibit the most severe plastic deformation. Correspondingly, Fig. 4 compares dislocation substructures typical for the unimpacted projectile (Fig. 4a) and a region near X in Fig. 3c (Fig. 4b). The TEM image in Fig. 4b shows very dense dislocation cells with heavy wall structures. Fig. 4 provides a reasonably accurate representation of the extremes in deformation

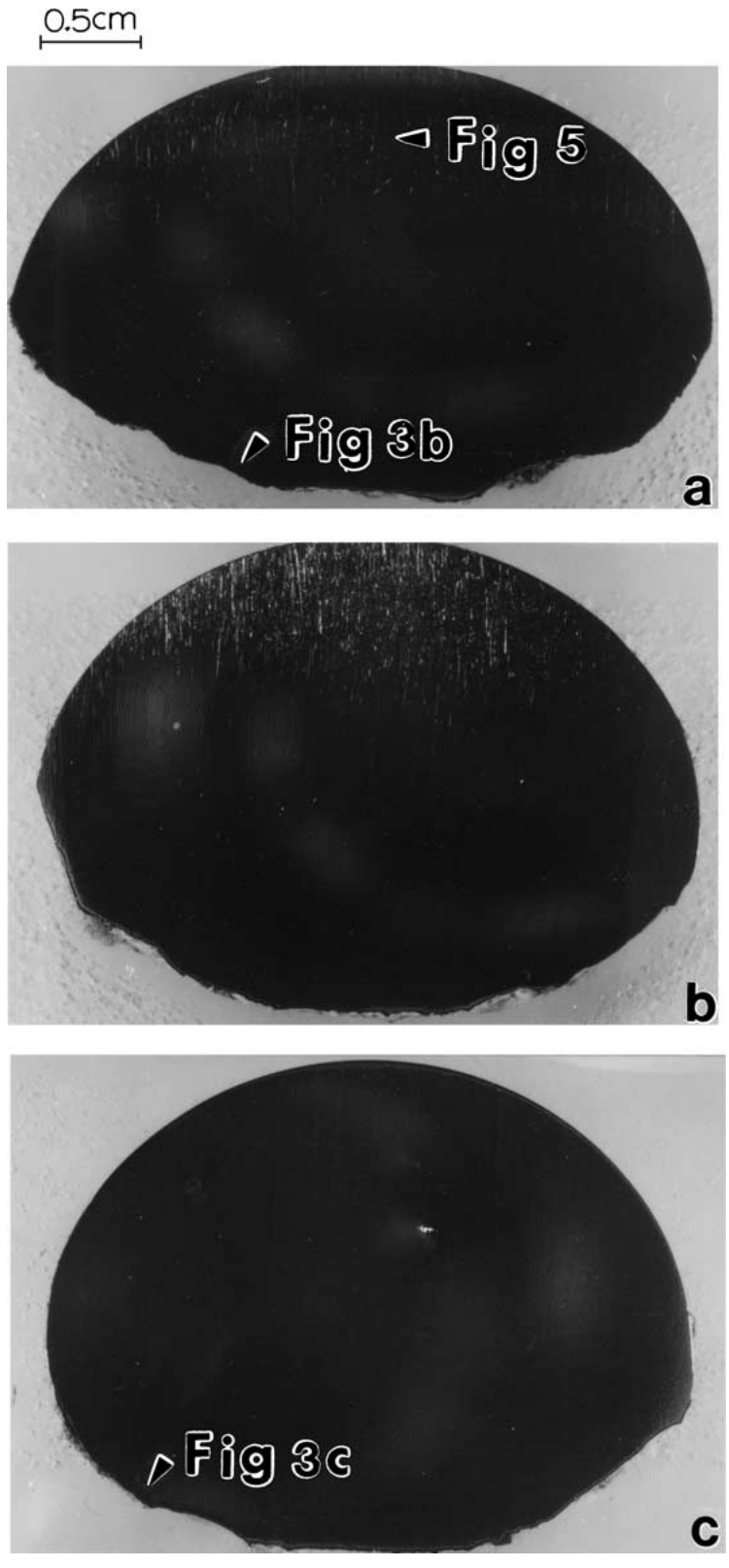

Figure 2 Experimental, recovered aluminum alloy half sections. (a) 0.8 km/s impact, (b) 1.0 km/s impact and (c) 1.3 km/s impact.

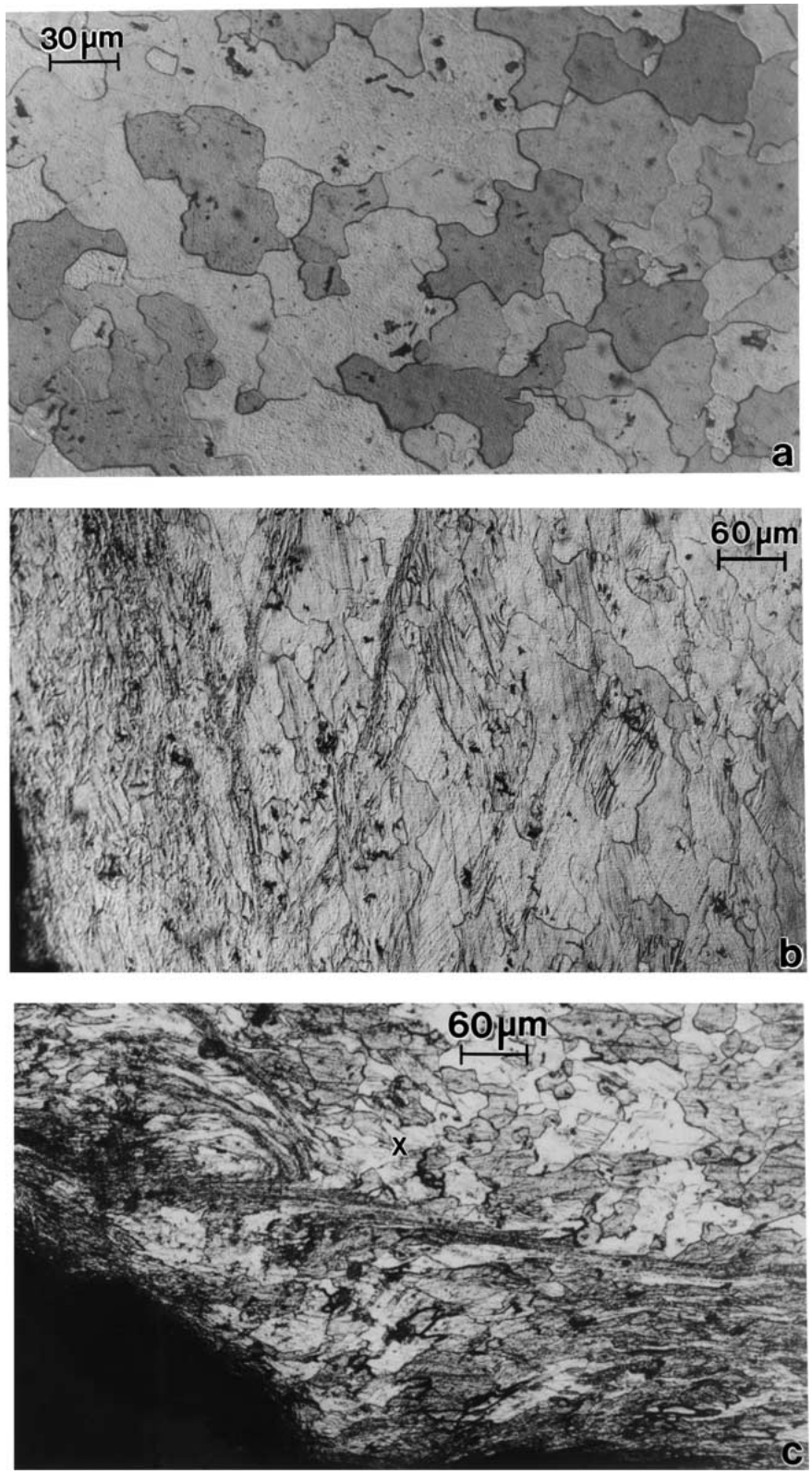

Figure 3 Representative microstructures observed in the aluminum-alloy sections shown in Fig. 2. (a) Near the center of half-section for unimpacted sphere showing generally equiaxed grain structure. (b) Deformation zone near projectile edge at 1.0 km/s impact; marked by arrow in Fig. 2a. (c) Deformation and shear-band like zone near projectile edge at 1.3 km/s. Marked by arrow in Fig. 2c.

microstructures observed in the impacted 2024 aluminum projectiles.

It can be noted in Fig. 3b and c that the grain structures away from the actual contact zone (showing severe deformation) are largely undeformed or undistorted (compare with Fig. 3a). Consequently the bulk of the recovered projectiles shown in Fig. 2 are not severely deformed. In fact, the macroscopic (biaxial) strain represented in each impacted projectile in Fig. 2 can be approximated from their deviation from a perfect 1.9 cm diameter sphere (or circle in projection or half section). Maximum strains of $\varepsilon_1 = 0.5$ and $\varepsilon_2 = -0.13$ are observed in Fig. 2a. These macroscopic strains are somewhat less than local strains characterized by the dense dislocation cell structures observed in Fig. 4b [2, 14]. In fact, consistent with previous observations

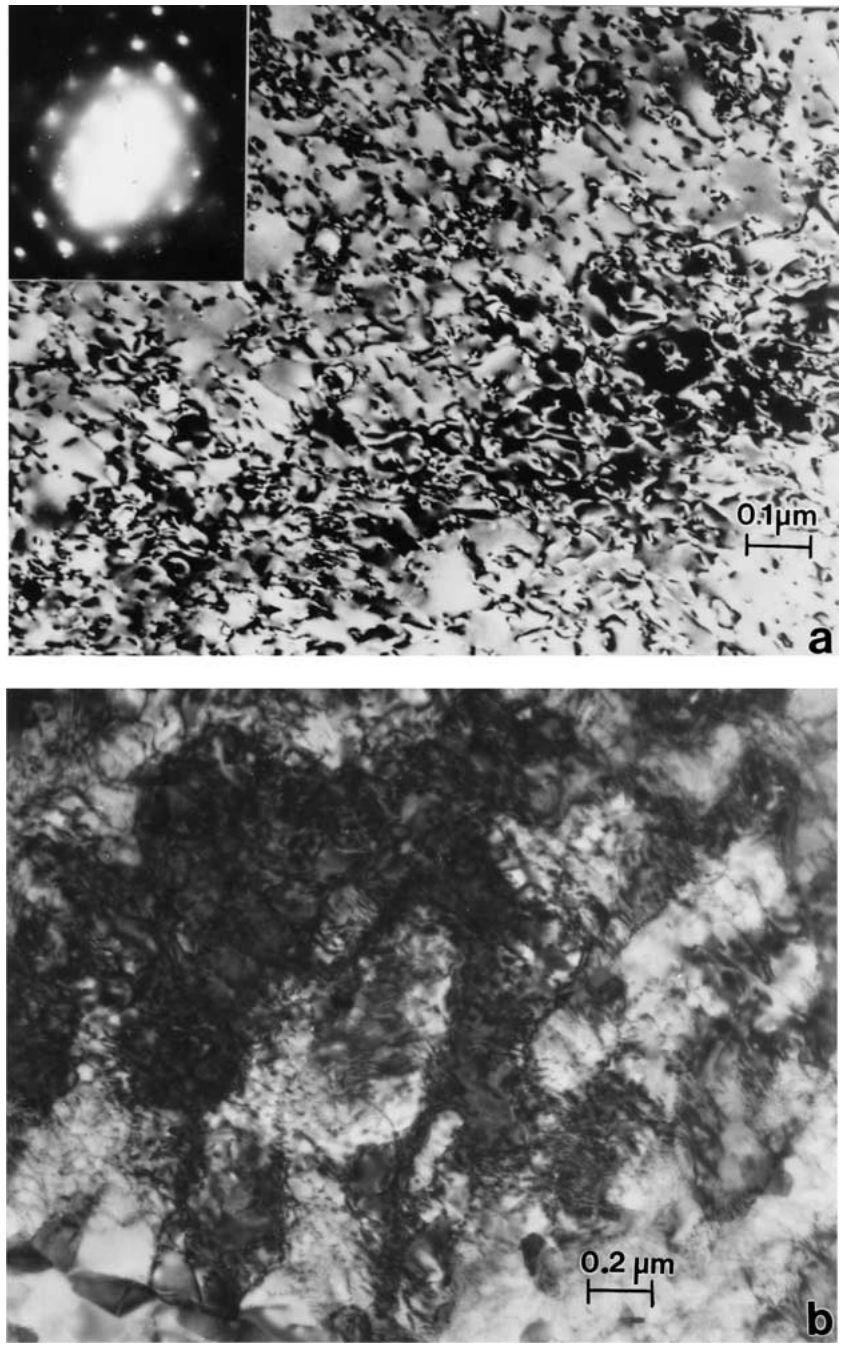

Figure 4 TEM images comparing dislocation substructures in unimpacted aluminum alloy sphere (a) (in region within Fig. 3a above) and region marked x in Fig. 3c above representing high dislocation density for 1.3 km/s impact (b). The grain surface orientation in (a) and (b) was (110) as illustrated in the selected-area electron diffraction pattern insert in (a).

of sub-surface stresses (or strains) resulting by particle impact erosion damage, etc., the dislocation substructure density and dislocation cell size decreases with distance away from the contacting (or contacted) surfaces [2, 3, 14]. In the case of the impacted projectiles in Fig. 2, the contact itself is observed to be nonuniform; consistent with impact phenomena in general [3, 14]. However the extent of contact and the contact radius (a_m in Fig. 1) could be fairly accurately measured from Fig. 2.

In addition to the local (Fig. 3b and c) and macroscopic (Fig. 2) deformation of the impacting projectiles, shock-wave induced spall effects were also observed near the back surface of the projectile impacted at 1.3 km/s. These effects were visible in the polished and etched cross-section as small cracks associated with the linking of voids (or void coalescence) in a region roughly 2 mm from the top or back surface. Fig. 5 illustrates this phenomenon. The shock wave originating at the point of impact of the 1.9 cm diameter 2024 aluminum sphere (at 1.3 km/s) with the limestone target propagates as a spherical wave (with a peak pressure of 11 Gpa utilizing Equation 6 [15]) toward the projectile (spherical) surface. The maximum pressure wave along the impact axis (Fig. 1) reflects from the top of the projectile and the interaction of the original shock wave and the release wave creates a tensile regime where the voids are created. Moreover, this regime as shown in Fig. 5 is not plastically deformed in the way the contact or impact surface-related zones are deformed;

Figure 5 Void coalescence and spall cracks near the top (back) surface in the 1.3 km/s projectile (Fig. 2c) (approximately 2 mm on the impact axis as shown by arrow).

as illustrated in Fig. 3b and c. This feature (Fig. 5) is a deviation from the microstructures created below an impacted, plane target surface (Fig. 1a). However, the behavior of the impacted projectiles shown in Fig. 2 (for an impact velocity range of 0.8 to 1.3 km/s) is largely elastic or elastic-plastic. The impact at 1.3 km/s and corresponding to a peak pressure of 13 GPa essentially represents the critical spall pressure. However, at higher impact velocities the accompanying projectile deformation dominated and the spall cracking is superseded. This prevents the material from fragmenting.

It might also be noted that in the early stages of high velocity impact the contact periphery moves supersonically in liquid/solid impact and has been reviewed recently by Field [19], and the effects in metals such as copper were discussed by Andrews and Field [20]. However there is not the degree of flow observed for the experimentally impacting Al 2024 spheres although the simulations illustrate a greater degree of plastic flow. These features are illustrated on comparing Figs 6 and 7.

Fig. 6a shows the results of microhardness mappings over the half sections represented in Fig. 2; with hardness values converted to corresponding residual yield stresses considering $\sigma_y \cong H/3$. The computed residual yield stress maps for corresponding impact projectiles are also shown for comparison along with computed extrapolations to higher (1.6 and 1.8 km/s) and lower (0.75 and 0.7 km/s) impact velocities in Fig. 6b. In Fig. 6b the projectiles have all been removed from the target as they were in the original impact experiments (Fig. 2). The plastic deformation effects which dominate the projectile development are illustrated in the computations. Fig. 7 shows an impact sequence for the projectile impacting at 1.8 km/s in order to provide a more complete context for the 2024 aluminum projectile impacting a semi-infinite, plane, limestone target. The lack of spall effects at this impact velocity are apparent.

It can be observed in both the experimental and computer simulated residual stress maps in Fig. 6, and in the simulated sequence of Fig. 7, that a maximum residual stress regime occurs within the impacted projectile,

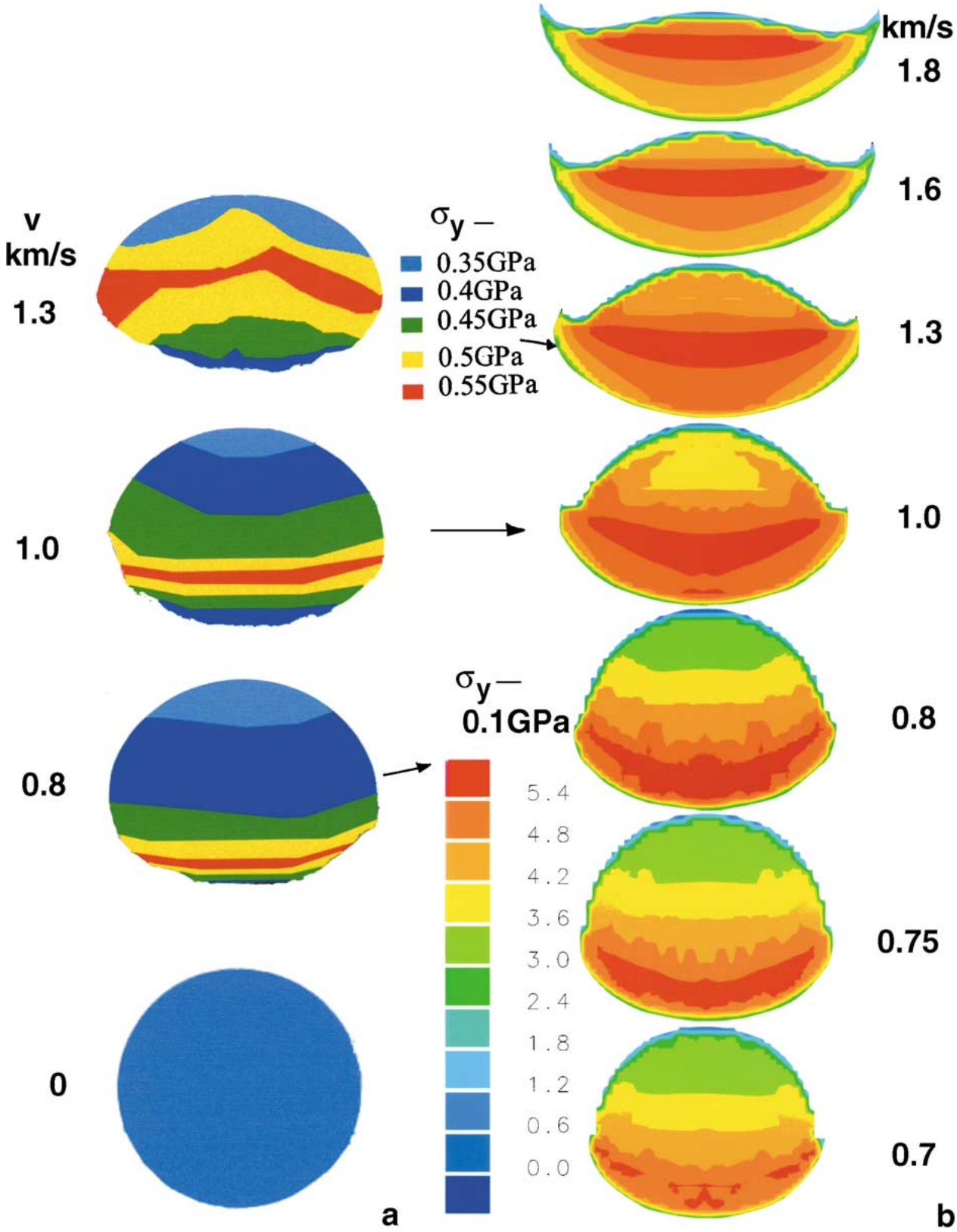

Figure 6 Experimental (a) and computer simulated (b) residual yield stress maps for aluminum-alloy 2024 1.9 cm diameter spherical projectiles impacting limestone targets at velocities shown in km/s.

behind the impact or contact surface. This regime moves away from the point of contact with increasing impact velocity in Fig. 6 and with the progression of penetration of the projectile with time in Fig. 7. Fig. 7 also illustrates the development and migration of a maximum residual stress in the plane target as well. However, the maximum stress is lower for the elastic target than for the projectile.

Consistent with Equation 1 the contact radius (a_m) measured from both the impacted experimental projectiles and the computed impact sequence in Fig. 6 increases with impact velocity, v. This data is compared in Fig. 8a. The maximum residual stress, measured at the center of the red zone in both the experimental projectiles and the computer simulated projectile impacts in Fig. 6 essentially saturates at 0.75 km/s and then, as

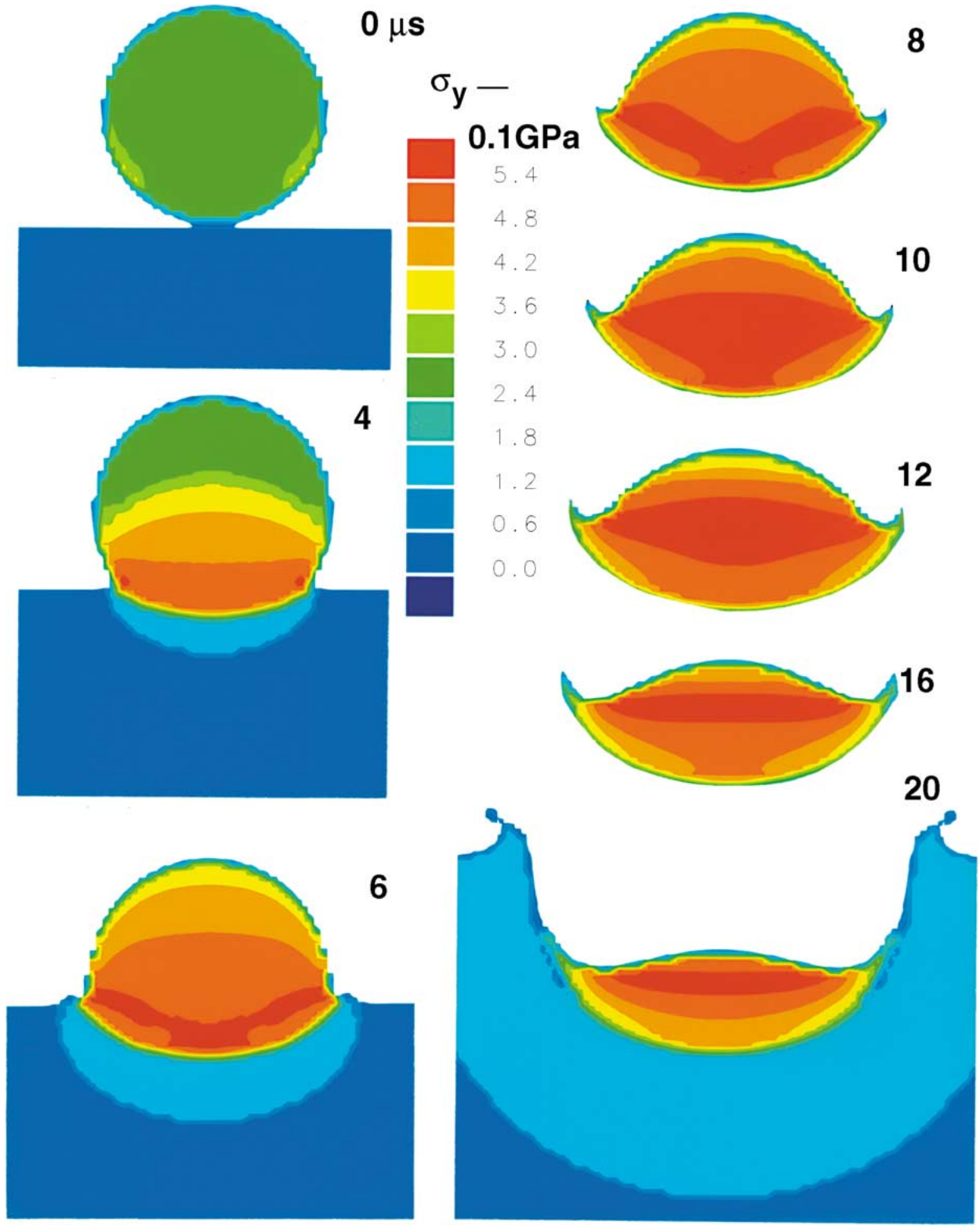

Figure 7 Computer simulated impact sequence for 1.9 cm diameter aluminum alloy (2024) spheres impacting a plane limestone target at 1.8 km/s. Times after impact in microseconds. Residual yield stress regimes are noted in the color key insert.

indicated above, migrates to the back surface of the deforming projectile. Fig. 8b and c illustrate the maximum residual stress migration by plotting z'_{max} normalized by the corresponding value of a_m, and the actual projectile height (or dimension along the impact axis, z_o shown in Fig. 1b) as a function of impact velocity. There is good correspondence between the three experimental projectiles and the computed projectiles in the data plots of Fig. 8b and c. Also consistent with the actual plastic deformation of the projectile, the overall residual stress (and hardness; or stored energy in the particle volume) increases with increasing impact velocity, and with time of penetration in Figs 6 and 7 respectively, as would be expected.

Figs 9 and 10 summarize the residual stress profiles mapped in Figs 6 and 7. Fig. 9 compares the residual stress as a function of the normalized distance into the impacting particle (z'/a_m) for the three experimental impact velocities where the maximum residual stress is observed to be very close to $z'_{max}/a_m \cong 0.5$.

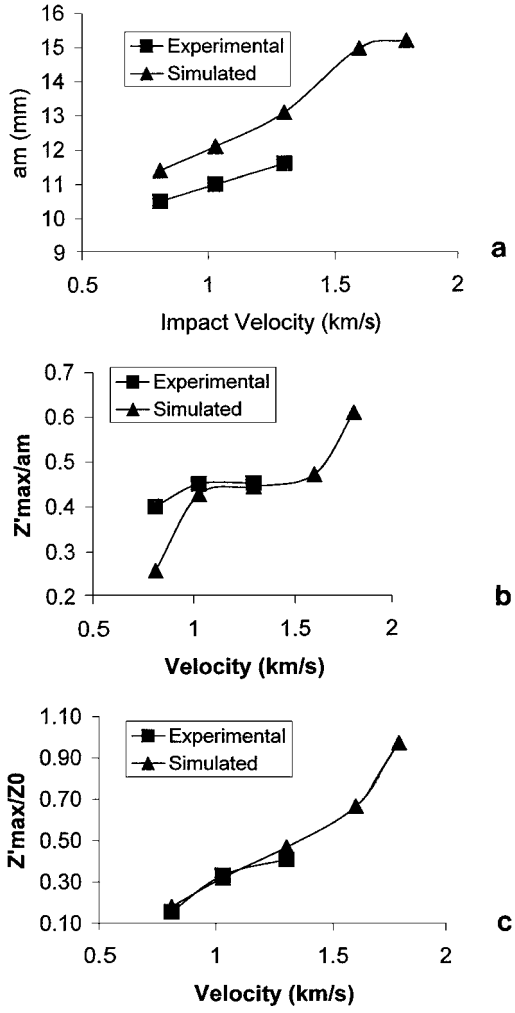

Figure 8 Comparison of experimental and simulated (calculated) axial (normal) impact parameters versus impact velocity. (a) Contact radius (a_m) versus v, (b) z'_{max}/a_m versus v, (c) z'_{max}/z_o versus v.

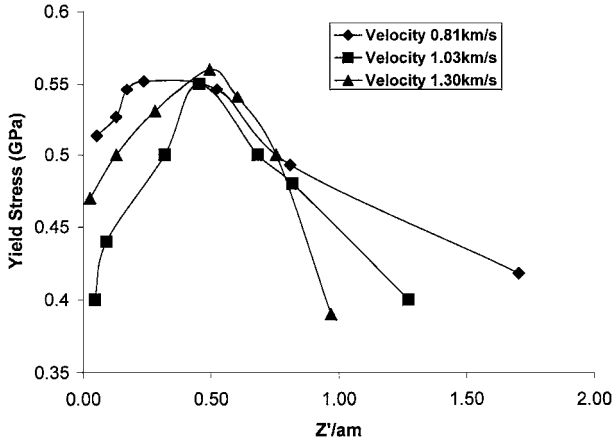

Figure 9 Comparison of residual yield stress values versus z'/a_m for the experimental impact velocities.

Fig. 10 compares the experimental and computed residual yield stresses with distance from the impact surface (z'); as a function of the experimental impact velocities. The occurrence of the maximum residual stress as demonstrated in Figs 8 and 9 is essentially the same as that shown for the maximum residual stress below a plane, impacted surface [3, 8, 14].

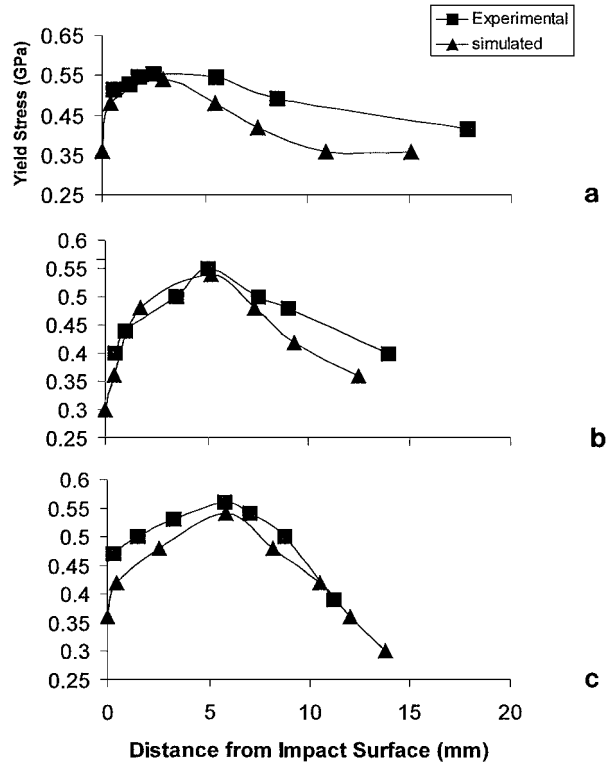

Figure 10 Comparison of experimental and computed residual yield stress values as a function of the distance, z', from the impact point along the impact axis (Fig. 1b).

6. Conclusions

A maximum residual stress phenomenon was observed for spherical aluminum alloy projectiles impacting plane, limestone surfaces over a velocity range of 0.8 to 1.3 km/s, and computer simulations extended this impact velocity range. The maximum residual stress was observed to migrate to the back of the impacting projectiles with increasing impact velocity. Comparison between the numerical (computer simulated) results and the experimental values of residual stresses revealed very satisfactory agreement in spite of the prominent plastic deformation of the impacting projectiles; especially above 1.3 km/s where the maximum strain is 50%.

Acknowledgment

This research was supported in part by NASA-Johnson Space Center Grant NAG-9-1100 and NASA-MURED Grant NAG-9-1171. F.M.R. was supported by a Fulbright Fellowship and L.E.M. was supported in part by a Mr. and Mrs. Macintosh Murchison Endowed Chair at the University of Texas at El Paso. We are grateful to Dr. Fred Hörz of NASA-Johnson Space Center for conducting the impact experiments. We are also grateful to Professor Doris Kuhlmann-Wilsdorf (University of Virginia) for her critical reading of the manuscript.

References

1. L. K. IVES and A. W. RUFF, ASTM Spec. Tech. Publication 664 (ASTM, Philadelphia, PA, 1979) p. 5.
2. D. KUHLMANN-WILSDORF and L. K. IVES, *Wear* **85** (1983) 361.
3. A. KARIMI, M. MAAMOURI and J. L. MARTIN, *Mater. Sci. Engng.* A **113** (1989) 287.

4. M. GUAGLIANO, *J. Mater. Processing Tech.* **110** (2001) 277.
5. S. A. QUINONES and L. E. MURR, *Phys. Stat. Sol*(a) **166** (1998) 763.
6. C. KENNEDY and L. E. MURR, *Mater. Sci. Engng.* A **325** (2002) 131.
7. O. L. VALERIO, V. S. HERNANDEZ, S. A. QUINONES, L. E. MURR and F. HÖRZ, in "Fundamental Issues and Applications of Shock-Wave and High-Strain-Rate Phenomena," edited by K. P. Staudhammer, L. E. Murr and M. A. Meyers (Elsevier Science, Amsterdam, 2001) ch. 49, p. 383.
8. F. I. GRACE, in "Fundamental Issues and Applications of Shock-Wave and High-Strain-Rate Phenomena," edited by K. P. Staudhammer, L. E. Murr and M. A. Meyers (Elsevier, Amsterdam, 2001) ch. 54, p. 421.
9. J. C. LASALVIA, E. J. HORWATH, E. J. RAPACKI, C. J. SHIH and M. A. MEYERS, in "Fundamental Issues and Applications of Shock-Wave and High-Strain-Rate Phenomena," edited by K. P. Staudhammer, L. E. Murr and M. A. Meyers (Elsevier, Amsterdam, 2001) ch. 56, p. 437.
10. H. HERTZ, *J.f.d.reine u.angew. Mathematik* **92** (1918) 156.
11. A. E. H. LOVE, "The Mathematical Theory of Elasticity" (Dover, New York, 1927) p. 138.
12. R. M. DAVIES, *Proc. Roy. Soc.* A **197** (1949) 416.
13. S. TIMOSHENKO and J. H. GOODIER, "Theory of Elasticity" 2nd ed. (McGraw-Hill, New York, 1951).
14. D. KUHLMANN-WILSDORF, L. K. IVES and A. W. RUFF, in Proc. 6th Int. Conf. on Erosion by Liquid and Solid Impact, edited by J. E. Field and N. S. Corney, Royal Air Force Establishment, Farnborough, Hants, England, September, 1983, p. 42-1.
15. M. A. MEYERS, Dynamic Behavior of Materials" (J. Wiley & Sons, New York, 1994).
16. M. VON THIEL, A. S. KUSUBOV and A. C. MITCHELL, "Compendium of Shock-Wave Data, UCRC-50108," Vol. 1, Supp. 1 (Lawrence Radiation Laboratory, University of California, Livermore, CA, 1987).
17. J. A. TYBURCZY and T. J. AHRENS, *J. Geophys. Res.* **92** (1986) 4730.
18. B. A. IVANOV and A. DEUTSCH, *Planetary Sci.* **XXXII** (2001) 1740.
19. J. E. FIELD, *Wear* **233–235** (1999) 1.
20. D. R. ANDREWS and J. E. FIELD, *J. Phys. D: Appl. Phys.* **15** (1982) 571.

Received 18 March
and accepted 4 September 2002